Detection of aerosol and cloud features for the EarthCARE lidar ATLID: the A-FM product

Gerd-Jan van Zadelhoff[1], David P. Donovan[1], and Ping Wang[1]

[1]Royal Netherlands Meteorological Institute (KNMI), de Bilt, the Netherlands

Correspondence: Gerd-Jan van Zadelhoff (zadelhof@knmi.nl)

Abstract. The EarthCARE satellite mission's objective is to retrieve profiles of the aerosol and water cloud physical properties using the combination of cloud-profiling radar (CPR), high spectral resolution UV lidar (ATLID), and passive multi-spectral spectral imager (MSI) data. Based on synergistic retrievals using data from these instruments, the 3D atmospheric cloud/aerosol state is estimated, which then are used to forward modelled radiative properties, which may then be compared to co-incident broad band radiometer (BBR) measurements. A high spectral resolution lidar enables the independent retrieval of extinction and backscatter but, being space-based, suffers from relatively high signal-to-noise levels. The ATLID FeatureMask (A-FM) product provides a probability mask for the existence of atmospheric features within the lidar profiles. Next to this, it also identifies those regions where the lidar beam has been fully attenuated and when the surface has impacted the measured lidar backscatter signals. From the pixels assigned as clear sky with no features present above, the clear sky averaged profiles for the three ATLID channels, the co-polar Mie channel, the total cross channel and the co-polar Rayleigh channel, are created. These 'feature-free' or 'clear-sky' profiles are useful for e.g. the quality of the ATLID l1 attenuated backscatters. The scientific goals of the A-FM product is to guide smoothing strategies within the ATLID profile retrieval algorithm which is one step further in the EarthCARE L2 processing chain. As a secondary product a frame-by-frame evaluation of the ATLID L1b cross talk calibration can be preformed by comparing the retrieved clear sky profiles to the expected channel profiles. The A-FM algorithm has been evaluated thoroughly using the synthetic test scenes. The A-FM product has been applied to both synthetic data from the EarthCARE end-to-end simulator (ECSIM) ass well as ALADIN L1 data from the Aeolus wind-lidar mission. Comparisons against the ECSIM model truth indicate A-FM has a percentage correctness >0.9 and is capable of reliably detecting aerosol and cloud regions with extinctions > 1E-5 m^{-1}.

1 Introduction

The EarthCARE mission (Earth Clouds, Aerosols and Radiation Explorer; (Illingworth et al., 2015) is a collaborative Earth observation satellite between the European Space Agency (ESA) and the Japan Aerospace Exploration Agency (JAXA). The satellite is planned to be launched in 2024 and its primary mission is to improve our understanding of the interaction between clouds, aerosols and radiation, and how these interactions affect climate and weather. The platform comprises a 94 GHz Doppler cloud profiling radar (CPR), the 355 nm high spectral resolution atmospheric lidar (ATLID), a multispectral imager (MSI), and a broadband long- and short-wave radiometer (BBR). EarthCARE science is built around the synergistic use of

these four advanced sensors (Eisinger et al., 2022) in order to estimate the 3D atmospheric properties of clouds, aerosols and precipitation, including their optical and microphysical properties. Forward modelled radiative properties of the retrieved 3D atmospheric fields can subsequently be compared to the BBR measurements for near-real time evaluation of the performed retrievals (Barker et al., 2022). In order to achieve these aims, a chain of individual instrument geophysical algorithms (L2a) and (L2b) synergistic (e.g. multi-instrument algorithms) have being developed (Eisinger et al., 2022). All the EarthCARE algorithms are realized as standalone processors, but are designed to fit into the overall retrieval process as their outputs are used as high level inputs, i.e. a priori settings, for algorithms present later in the chain.

A lidar feature detection mask is a mask used to identify different atmospheric features, such as clouds or aerosols. Next to this it, also identify regions where the lidar beam has been attenuated or when the ground surface has an impact on the measured lidar backscatter signals. For all lidar instruments which suffer from relatively low signal-to-noise rations (SNR), which includes all space missions, a type of feature mask has been developed. These are needed to provide context to the lidar signals. In this paper, the ATLID FeatureMask(A-FM) L2a retrieval algorithm developed for the ATLID instrument is described, as well as the evaluation using synthetic model fields and the Aeolus data.

The Cloud-Aerosol Lidar and Infrared Pathfinder Satellite Observations (CALIPSO; Winker et al., 2009) was launched on April 28, 2006 in order to study the impact of clouds and aerosols on the Earth's radiation budget and climate. The CALIPSO lidar, the Cloud-Aerosol LIdar with Orthogonal Polarization (CALIOP), is an elastic backscatter lidar that emits linearly polarized laser light at 532 and 1064 nm and receives both the linear polarized signals and the cross polarized signals at 532 nm.

For the CALIPSO lidar (Winker et al., 2009), there are two similar feature-mask type products. The first is the Vertical Feature Mask (VFM; Vaughan et al., 2009), currently at Version 4-21, which describes the vertical and horizontal distribution of cloud and aerosol layers observed by the CALIOP lidar. The VFM mask discriminates aerosols and clouds based on their physical feature differences within an (averaged) profile. The need to discriminate aerosols and clouds requires relatively large horizontal averaging windows of profiles at native resolution $\frac{1}{3}$ km up to 80 km. The second CALIOP product is more recent, and retrieves "context-sensitive" features within the signals using 2-D image information from neighboring lidar profiles (Vaillant de Guélis et al., 2021). It uses the backscatter signals from all three available CALIOP channels and iteratively determines lower thresholds to find weaker features within the image. The main advantage of this method is that the complex shapes of aerosol and cloud features are better preserved and masked. Even though the method implemented is different the basic idea of using image reconstruction techniques is similar to the method described in this paper.

Another new approach has been created for the NASA ICESat-2 mission, which carries the space-borne lidar system ATLAS (Markus et al., 2017) operating at 532 nm. The aim of this mask (Herzfeld et al., 2021) is to detect layers in the ICESat-2 data during complex atmospheric situations, specifically aiming at the detection of blowing snow and thin cirrus clouds. The method adopts a Gaussian radial data aggregation function with an auto-adaptive threshold determination.

The A-FM provides a probability of whether a pixel contains cloud and/or aerosols, it does not perform any typing information of the respective pixel at this point. The main goal for both 2-D approaches for CALIOP and ATLAS are the same as that for the FeatureMask detection algorithm described within this paper. In contrast, the VFM algorithm retrieves typing

60   information of the aerosol and cloud returns, which requires a far higher Signal to noise ratio (SNR). The cloud and aerosol classification of any identified features is performed at a later stage in the EarthCARE L2 chain.

Both CALIPSO and ICESAT-2 operate elastic backscatter lidars, whereas ATLID is an high spectral resolution lidar (HSRL). To benefit from the HSRL ability to directly retrieve extinction and backscatter separately, correct averaging of the data is essential. To assist in the smoothing strategies performed in the ATLID profile retrieval algorithm (A-PRO; Donovan et al.,

65   2022b) a mask at the highest possible resolution is needed where strong (liquid layers, optically thick ice clouds, optically thick aerosols regimes and surface returns) and weak back-scattering regions (aerosol fields and thin ice clouds) are well separated from each other and clear sky regions. This to ensure that signals from liquid clouds signals are not mixed with aerosol of cirrus layers. These smoothed signals would result in incorrect extinction retrievals which do not represent the actual atmospheric state leading to e.g. an incorrect target classification in A-PRO.

70   The effects of the A-FM processor output carry throughout the chain. Since the smoothing strategy in the ATLID profile retrievals is based upon the detected features it defines the regions where retrievals are applied. This information is subsequently carried into the synergistic lidar-radar target classification (Irbah et al., 2022) and therefore synergistic cloud and aerosol property retrieval algorithm ACM-CAP (Mason et al., 2022).

For the testing of all the EarthCARE processors a number of detailed simulated scenes have been created, using as input

75   a number of atmospheric states calculated by different NWP models. These model states were subsequently transformed into EarthCARE Simulator scenes after which realistic L1b signals were calculated, for a full description of these scenes seeDonovan et al. (2022a). Within this paper we focus on the so called 'Halifax-scene' and a sub-set of this scene focusing on the aerosol regime for the evaluation of the A-FM processor.

In Section 2 we provide a detailed description of the FeaturMask detection of area's with aerosol and/or cloud particles. In

80   Section 3 the performance and sensitivity of the procedure is described using simulated EarthCARE L1b data and corresponding model truth from the evaluated test scenes.

In August 2018 the European Space Agency (ESA) launched the Aeolus Earth Explorer Mission (Reitebuch et al., 2019), carrying the first space-based Doppler wind lidar. The main instrument on board is an ultraviolet UV high-spectral resolution lidar, the Atmospheric LAser Doppler INstrument (ALADIN). Even though the focus of Aeolus is on the retrieval of line of

85   sight winds the instrument measures atmospheric profiles of Mie and Rayleigh attenuated backscatter signals. The combination of A-FM and A-PRO developed for the inversion of ATLID signals has been rewritten for the Aeolus mission. These versions, named AEL-FM and AEL-PRO respectively, are currently part of the Aeolus operational processing stream. In the case of AEL-FM, the main difference with respect to A-FM has to do with oversampling the 24 vertical bins of Aeolus data to a higher vertical resolution in order to to enable the use of the A-FM procedures described below. Once the input has been regridded,

90   AEL-FM and A-FM are in essence similar, and only once the output has been created at high resolution it needs to be remapped to the Aeolus measurement grid. In Section 4 the results for the the Halifax test scenes and one Aeolus-CALIOP collocated orbit are presented. Finally, the conclusions are presented in Section 5.

2 FeatureMask Retrieval algorithm

2.1 Algorithm background

95   The A-FM algorithm determines the feature detection probability mask based on exploiting the time-height correlation of the data while using a minimum number of hard coded or input dependent thresholds. The main reason for this approach is to enable the retrieval to deal with the low signal to noise ratios associated with ATLID signals at the single-pixel level. Since A-FM retrievals are used to guide smoothing techniques and windows in later processors, the first goal is to separate 'strong' features from 'weaker' features. Two complementary methods are employed in the algorithm to retrieve the feature mask: the median-

100   hybrid method (Rush, 2007, chapter 4) for strong features, and a data smoothing strategy based on a simplified maximum entropy method(Smith and Grandy, 1985) for the detection of weaker features. It was found that employing the maximum entropy method is both too time consuming and does not always converge to a single optimal smoothed image. In general it was deemed to focus too much on the stronger features in the noise while missing some of the more tenuous widespread aerosol layers. To ensure that the algorithm is robust and fast enough for the usage of space-based data, the algorithm has been

105   simplified and now uses 3 or 4 pre-defined convolved images, instead of attempting to retrieve the rigorous, maximum entropy defined image. These four convolved images span the entire parameter space in which any optimum maximum entropy image has been identified in the evaluation period of the algorithm. Based on these two methods, coherent atmospheric structures are defined, dubbed as features within this work.

The lidar deployed on the EarthCARE satellite (ATLID) is a high-spectral-resolution (HSRL) depolarization lidar operating

110   at a wavelength of 355 nm, see Wehr et al. (2022) for an elaborate description of the mission and ATLID instrument. In the ATLID instrument, the incoming signals first pass through a polarised beam splitter separating the cross-polar signals from the co-polar signals. The co-polar contribution in the return signal is subsequently separated into contributions from the thermally broadened molecular (Rayleigh) return and the spectrally narrow elastic backscatter returns from cloud and/or aerosol particles by means of a Fabry-Perot Etalon based spectralfilter. Within the EarthCARE terminology, the former signal is referred to as

115   the co-polar Rayleigh return and the latter as the co-polar Mie return. The two measured signals are not fully separated since the Etalon is not an ideal filter. To separate the contributions of 'Mie' signals in the Rayleigh channel and vice versa a cross-talk correction is applied within the L1 processor (Eisinger et al., 2022; do Carmo et al., 2021). For the cross polar channel the Mie

and Rayleigh signals are not separated. After these correction and an absolute calibration (and ignoring multiple-scattering contributions), the three ATLID channels can be related to the atmospheric extinction and backscatter signals as:

$$P_R(z) = \frac{\beta_R(z)}{r^2(z)} exp\left[-2\int_{z_{lid}}^{z}(\alpha_M(z') + \alpha_R(z'))dr'\right],$$

$$P_M(z) = \frac{\beta_M(z)}{r^2(z)} exp\left[-2\int_{z_{lid}}^{z}(\alpha_M(z') + \alpha_R(z'))dr'\right], \tag{1}$$

$$P_{T,\perp}(z) = \frac{(\beta_{M,\perp}(z) + \beta_{R,\perp}(z))}{r^2(z)} exp\left[-2\int_{z_{lid}}^{z}(\alpha_M(z') + \alpha_R(z'))dr'\right],$$

where P_R is the Rayleigh co-polar attenuated backscatter, P_M is the Mie co-polar attenuated backscatter and P_T is the total cross-polar attenuated backscatter. z is the atmospheric altitude and $r(z)$ the range from the lidar. α_M is the combined aerosol and cloud extinction and α_R the atmospheric Rayleigh extinction. β_M is the co-polar Mie backscatter, β_R is the co-polar Rayleigh backscatter, $\beta_{M,\perp}$ is the cross-polar Mie backscatter and $\beta_{R,\perp}$ is the cross-polar Rayleigh backscatter. The atmospheric Rayleigh extinction and co-polar Rayleigh backscatter are directly related to each other and depend both on the local molecular density.

When the atmospheric state, i.e. pressure, temperature and therefore molecular density, is known, the only remaining unknown parameter in the P_R [Eq. 1] is the aerosol and cloud extinction profile, which can therefore be independently retrieved from the aerosol and cloud backscatter ($\beta_M(z)$) profile. This ability to perform independent retrievals of the backscatter and extinction profiles is the major improvement with respect to that from an elastic backscatter lidar like CALIPSO (Vaughan et al., 2009) or ICESaT-2 (Herzfeld et al., 2021) for which an extinction-to-backscatter ratio has to be assigned for each pixel.

Before the aerosol and cloud extinction are retrieved it is usual to check where aerosol and clouds can be detected, i.e. a feature mask needs to be created as an input to the extinction retrieval algorithm. In an noiseless and well calibrated HSRL system, the detection of aerosols and clouds may be performed by calculating the backscatter ratio, which is the ratio of the total signal with respect to the Rayleigh:

$$\frac{(P_R + P_M)}{P_R} = \frac{(\beta_R + \beta_M)}{\beta_R} \tag{2}$$

Since both signals depend similarly on the extinction and distance, the exponential term and range dependence cancels out when calculating the backscatter ratio. When the ratio is greater than 1 there are aerosol or cloud particles in that pixel when it is very close to 1 the return consists of molecular backscatter signal only and enable the start of high resolution retrievals of the extinction and the unattenuated backscatter profiles.

This does not work as easily in reality since noise is present. In the case of the EarthCARE lidar ATLID, the Mie signals are separated from the total signals by a Fabry-Perot etalon. Due to this configuration, a large noise component is present in both the Mie and the Rayleigh channels, referred to as cross-talk. Specifically, cross-talk is Mie signal which ends up in the Rayleigh channel and vice versa. The cross-talk combined with the more standard noise sources (background, dark count,

145 element efficiencies), hampers the above described backscatter ratio method based on signal to noise ratios which is more generally used for ground based or airborne HSRL systems. It is still possible to apply such methods for the ATLID signals, but would only enable the detection of high SNR signals and therefore very optically thick ice clouds and water clouds. When one aims to detect aerosol and thin cirrus cloud regions, the signals would have to be smoothed so drastically that most of the information content is lost if this is done blindly when averaging strong and weaker signals.

150 An example of the expected ATLID signals are presented in Figure 1 for the Halifax-aerosol scene, over the Caribbean, consisting of an ice cloud, a thick aerosol layer (with an AOD $\approx$0.28) and a thin aerosol layer between 4 and 6 km height ($\tau \approx$ 2.2e-2). The region is part of the Halifax scene with an enhanced marine aerosol optical thickness (Donovan et al., 2022a). Note that the absolute attenuated backscatter values in the clear sky (color of the noise pixels) are similar to the strength of the elevated aerosol layer (1, panel 2). Simply thresholding will not work in this case. The main difference between the two

155 regimes is that the aerosol field shows a more coherent horizontal and vertical field compared to the high spatial variability in the clear sky regions. The attenuation is clearly visible in the Rayleigh channel below the ice clouds, the ice clouds themselves are seen in both the co-polar Mie channel and the total Cross polar channel. In most cases it will not be possible to mask aerosol layers on an isolated shot-by-shot basis, i.e. as is visible in especially the elevated layer between 4 and 6 km. To enable the detection of these optically thin layers the data needs to be smoothed, however the backscatter signals strength from different

160 target can differ up to a factor of 100. Any smoothing strategy needs to take this into account to not combine information from strong and weak returns resulting in the retrieval of inconsistent particle properties.

If the noise in the HSRL system is reasonably unbiased and uncorrelated, e.g. if there is no preferred height or positional relation for the cross-talk, one can treat this as true noise, additionally the signals in the Mie channel, after accurately accounting for cross-talk, arise from cloud or aerosol particles and not from air molecules. In general, particle features are not single pixel

165 events, but extend in both the vertical and horizontal directions. The combination of these two features (unbiased uncorrelated random noise and pure extended particular signal) point to the use of image reconstruction techniques. These techniques can implicitly take into account information from surrounding pixels. Within the ATLID-FeatureMask processor a combination of two techniques have been applied; the hybrid median method to detect strong features and smoothing of the remaining low SNR data to enable the detection of weak features.

170 ## 2.2 FeatureMask definition and Overview

The FeatureMask main output is a feature detection probability index ranging between 0 (clear sky) and 10 (likely very thick clouds). The mask does not separate between different particle types but does intend to separate area's of strong returns, weak returns and clear sky regions. The A-PRO processor (Donovan et al., 2022b) digests these inputs and defines signal smoothing strategies based on the defined probabilities. In table 1 the definition of the FeatureMask is provided with a short

175 and long description of each of the possible values. The meaning and description of the values should not be interpreted in a qualitative sense. The description is solely based upon what is to be expected based upon the absolute signals and their signal-to-noise ratios. High backscatter returns in general come from optically thick ice clouds and liquid layers, whereas most aerosol cases show lower backscatter values. The detailed lidar target classification is performed in the A-PRO algorithm

, where the attenuated backscatter levels combined with temperature, extinction, depolarization, and lidar-ratio are used to
180 identify different cloud and aerosol types. The description of how each A-FM feature probability value is defined is given in
the following Sections.

Value	Meaning	Explanation
10	Thick Clouds	Mie signals are very strong indicating cloud returns from liquid or optically thick ice clouds
8-9	Thick aerosols or clouds	Mie signals are strong and most likely from clouds, although high optically thick aerosols can get to these values
6-7	Aerosol or thin clouds	Mie signals from optically thin (Cirrus) or attenuated clouds and aerosol regions should reside here.
5	Low altitude aerosols	Set to bins for which overlying aerosol features are most likely connected to the surface,
1-4	Likely clear sky	Low Mie signals, indicative of clear air, differences between these values are due to removed features after additional checks
0	Clear sky	Very low Mie signals expected to come from cleat air
-1	Attenuated	Fully attenuated pixels found through the Rayleigh channel signals
-2	No retrievals	Set in the case of a gap in signals or L1 data not trusted (due to calibration, miss-pointing or otherwise)
-3	Surface	pixel found by the surface retrieval, these may include pixels above the surface affected by the surface returns.

Table 1. FeatureMask definition with the first column showing the true output values from the algorithm. The second column provides a
hand waving classification and the third an explanation on how this should be interpreted.

From a usage point of view, data between 5 and 7 can be smoothed or grouped together when present in neighbouring pixels.
For any value between 8 and 10 care has to be taken before e.g. averaging with neighbouring points. The same holds for all
values below 0. The direct surface return (-3) can be substantially larger than a low level aerosol field. Any smoothing of a
185 (sub)surface point in the backscatter retrieval can have a large impact on the resulting retrieved values and subsequent retrievals
like aerosol type. Likewise adding clear sky pixel values in the smoothing effort will dilute the signals and can result in similar
incorrect type classification. For the retrieval of the weaker features of the FeatureMask a number of smoothing techniques and
statistical approaches are employed when determining dynamic thresholds. In the case of EarthCARE, an orbit is divided into
8 frames and within A-FM each frame is subdivided in horizontal along track blocks of around 1100 km, containing around
190 4000 profiles, with an overlap between the blocks of 100 profiles. These blocks are processed independently in parallel and
the results are combined just before the FeatureMask is written to the product file. This should ensure that, within each block,
enough pixels are available to enable statistical approaches and still have a similar enough atmospheric state. The size of the
blocks is configurable and will be evaluated once actual ATLID data is available.

In the case of missing profiles, either due to a problem in the calibration or a temporary lack of data, a choice has to
195 be made whether the features on both sides of these gaps can be considered continuous or should be treated separately. In
the case of aerosol fields, the spatial correlation lengths have been investigated by correlating backscatter profiles between
EARLINET groundstations and CALIOP overpasses (Grigas et al., 2015). This showed a 'fairly good' correlation of around
0.86 within a 100 km overpass radius. In the case of A-FM it is assumed that weak (aerosol) signals cannot be smoothed
beyond a conservative 60 km gap. When a gap exceeds this horizontal length the low signal to noise ratio data smoothing is
200 performed separately on each side of the gap.

2.3 Surface detection

The co-polar Mie backscatter signal from the surface can be significantly higher compared to the atmospheric returns just above the surface. With the horizontal and vertical smoothing of the data required to perform any retrievals for a noisy system like ATLID, all pixels which are contaminated by surface returns need to be masked out by creating a surface mask. The

205 starting point for this mask comes from the digital elevation model (DEM) height provided with the ATLID L1b data files. The ATLID signal has a vertical resolution of approximately 103 m with a vertical crosstalk of 11% up to 20 km altitude (do Carmo et al., 2021), i.e. 11% of the signal in a vertical pixel leaks into the neighboring pixels. Secondly, the onboard summing of two consecutive lidar profiles is envisaged as standard during the mission. Both effects can cause surface returns to propagate into the range bin above the DEM-surface and therefore find their way into the smoothed aerosol signals if not classified as such. To

210 ensure that no surface signals affect the smoothing of data, a conservative surface influenced height mask is defined on profile by profile basis. For each profile, first the co-polar Mie peak range-gate is located by searching up to 2 pixels above the one in which the DEM altitude is located. This 'surface-peak' has to be greater than $3\times$ the average signal noise in the co-polar Mie channel between 20 and 40 km. If the latter condition is not met, the beam is assumed to be attenuated and the surface pixel is set to the DEM pixel. Once the surface-peak (i_{surf}) has been assigned, the backscatter signal in the adjacent pixel above is

215 checked by comparing this to both the surface-value itself, the value at $i_{surf} + 2$ and the average of the Mie channel signals between $i_{surf} + 3$ and $i_{surf} + 8$. The surface height is raised one pixel when the following conditions apply:

$$
\begin{aligned}
\beta(i_{surf} + 1) &> 0.75 \times \beta(i_{surf}) \\
\beta(i_{surf} + 1) &> \overline{\beta(i_{surf} + 3 : i_{surf} + 8)} \\
\beta(i_{surf} + 1) &> 5 \times \beta(i_{surf} + 2)
\end{aligned}
$$

220

The first condition compares the signal with respect to the surface peak, the remaining two aim to evaluate whether the backscatter in the pixels above the surface is indeed higher than expected with respect to the pixels just above, or are part of a vertically extended above surface feature.

Once pixels are defined as being(sub-)surface they are no longer used in the subsequent feature detection procedures. The

225 main disadvantage of this could be that potentially, low and shallow features like fog and blowing snow can be missed and will not be reported as features but as surface. Once any of these features is more vertically extended the second and third condition are aimed to keep the surface at the highest Mie peak around the DEM. This part of the processor will be extensively evaluated once ATLID provides real data and updated to provide the best possible surface-mask and low height features while at the same time ensuring that surface backscatter is conservatively identified.

230 ## 2.4 Converting signals to signal probabilities

As was depicted in Figure 1, the dynamic range of backscatter signals can span a number of magnitudes within a small spatial difference for optically thick clouds, while having very similar signals for weaker features with respect to background noise

8

levels. In order to linearize the scale of the signal strength, signal probabilities are used within within the algorithm, which takes into account both the signal strength and its local noise. Here, the approach being used by the CALIOP team (Vaughan et al., 2009) is followed by assuming that Gaussian statistics are a reasonable approximation for the detected ATLID signals. If this is found not to be the case after launch, and the relevant information is available, this step can be updated to the correct statistical approach. Both the signals and noise levels for each of the three ATLID channels are available in the L1b products (Eisinger et al., 2022), where it is assumed that the noise level are defined as the signal standard deviations. In this case, the probability of detection can be calculated as

$$P_d = 1 - \frac{1}{\sqrt{2\pi}\sigma_s} \int\limits_{\sigma_s}^{\infty} e^{-S^2/2\sigma_s^2} ds \tag{3}$$

where S is the signal, σ_s the standard deviation of the signal and P_d the detection probability. This integral can be re-written using the error function ($erfc$) to

$$P_d = 1 - \frac{1}{2} erfc\left(\frac{S - \sigma_s}{\sqrt{2}\sigma_s}\right) \tag{4}$$

To enable the detection of very strong single pixel events, i.e. the direct backscatter from small optically thick (liquid) Cumulus clouds, the pixels with Mie signal probabilities very close to 1 (high signal with relatively low noise) are set within the Feature-mask (FM) index to a value of 10 (a virtual certain target detection).

2.5 Detection of strong features

Once the surface pixels are known, a hybrid median (HM) filter (Rush, 2007, Chapter 4) is applied to the the entire image on a pixel-by-pixel basis. the HM filter uses an n x m box, where n and m are odd integers greater than 5 and represent ATLID along-track and vertical range-gate pixels respectively. The size of the median filter (m) is configurable through a configuration file and two sizes of filters are applied, m×m and m×3 and the detected features are combined. The along-track oriented m×3 box sized filter specifically targets the detection of horizontally distributed 'thin' features e.g. strato-cumulus decks. This is described in more detail later within this section. In the examples shown within this paper, a value of 11 has been adopted for both n and m. This configuration parameter was shown to provide the optimal value for the detection of cloud edges and the filling of internal small feature-gaps using available test scene data. The operational value will be determined once the actual EarthCARE L1b data has been characterized and calibrated.

The value of the centre pixel returned by the HM filter is retrieved by calculating the median values of the two diagonals, the horizontal and vertical rows within this box, using the kernels in Figure 2, after which the median value of those four median values is determined. As this latter median is calculated from an even number of values, the third value of the sorted array (not the mean of two values in the centre) is used. Those pixels either flagged as (sub-)surface or non-valid L1b data are not calculated nor taken into account in the calculation of the median.

The HM filter is very effective in removing single noise events and filling small gaps within stronger features. As only median values are used, there are no smoothing edge effects. The hybrid median algorithm is run iteratively five times to

ensure that the image has converged, e.g. there are no more changes in the image between this iteration and the next. This
procedure is performed simultaneously for both the co-polar Rayleigh and co-polar Mie signals. Those pixels with a value
above a user defined threshold (within this paper a value of 34% is adopted) are set as a strong feature return. Those Rayleigh
pixels with a hybrid-median-value $< 40\%$ are set to be fully attenuated.

In Figure 2, examples of the HM filters used for detecting the strong coherent features are shown. All pixels with a The thick
lines depict those lines used for the median calculation for the grey center pixel.

The only coherent structures which will not be detected using the m×m kernel are structures with a vertical or horizontal
width of 1 or 2 pixels. Particularly, the detection of horizontally oriented 'thin' structures are at risk here since these will
be common for high optically thick water clouds (stratus or cumulus). These may yield only 2 pixel thick clouds before the
backscatter signal is completely attenuated. To insure the detection of these important structures, the hybrid median technique
is applied a second time using an m × 3 box ensuring that features of only two pixels thick, e.g. water clouds, are detected.

The results from the two different HM sizes filters are compared and the additional features in the m×3 hybrid median
results are added to the m×m mask. The square mask is considered to be the superior masking routine, as it takes into account
both vertical and horizontal coherence and is capable of filling in larger gaps. If only the m×3 version is used, the strong
features in 1 are still detected but with a higher variability and more 'noisy' behaviour within the features. The resulting
converged hybrid median results for the aerosol image seen in Figure 1 is depicted in Figure 3. The top panel shows the signal
probability after converting the co-polar Mie signals using Eq. 4 whereas the bottom panel show the resulting signals after 5
iterations of the hybrid-median filter procedure. The procedure is used for both the co-polar Rayleigh and co-polar Mie images.
The combination of signals in the co-polar Mie and total cross polar channel has been looked at but was discarded as a viable
option. There are three main reasons for this. Even though the detection of depolarizing features, i.e. ice clouds or dust-aerosols,
would benefit from this combination, the SNR of the combined signal would become lower for all other pixels. Secondly the
two channels are calibrated separately which can introduce a local bias for regions in between calibration targets, thirdly the
cross channel contains both particulate and molecular backscatter signals which will reduce the feature contrast, especially
closer to the surface where the molecular density is highest. The resulting Rayleigh mask (not shown) helps identifying those
regions for which the lidar signals are completely extinguished, while the co-polar Mie images are used to detect regions which
have aerosol or cloud particles.

The most important task of this part of the algorithm is to correctly detects edges with e.g. no smoothing beyond the features
or cutting corners. This will assist in defining the smoothing strategies used in the A-PRO (Donovan et al., 2022b) processor
and ensure that liquid signals will not be mixed with neighboring aerosol regions during signal binning/smoothing operations.

2.6 Detection of weak features

With the high signal to noise features determined, the next step is to search for coherent structures within the remaining part of
the co-polar Mie image. For this we start with the original co-polar Mie probability images ($P_{d,Mie}$ Eq. 4) and create the weak
feature probabilities ($P_{HM,Mie}$) image. The first step is to remove all the probabilities where strong features, (sub-)surface
and fully attenuated pixels were detected and swap these with realistic 'weak feature' values. To accomplish this, the previous

detected strong-feature pixels are filled in using a linear interpolated value of the averaged signals ($\overline{\beta}_{top,bot}$) above and below the already detected feature within the column. The $\overline{\beta}_{top}$ and $\overline{\beta}_{bot}$ values are calculated using a 5x5 box of the remaining

300    $P_{d,Mie}$ pixels. The sub-surface regions are filled in similarly with the lowest pixel set to the background noise value. The reason for this replacement strategy is to ensure that weaker edges of strong features (not detected by the HM procedure) are not fully smoothed out by the clear sky pixels surrounding them but have neighbouring pixels with similar strength.

As the most obvious features are already detected and only a noisy image remains, a very simple convolution method is needed to check for more coherent features within the noise. Within the algorithm the filled in $P_{HM,Mie}$ 2D-array is iteratively

305   convolved using a horizontally oriented 2-D Gaussian normalized Kernel, where the horizontal and vertical standard deviations (in pixel numbers) can be set by the user. In the ATLID examples provided in this paper values of (11 along-track ATLID pixels $\times$1.5 vertical range gates) are respectively used. The iterative smoothing is performed in Fourier space making each convolution a simple matrix multiplication. For four specific user defined iteration steps the inverse Fourier transformation is performed resulting in images of smoothed probabilities ($P_{i,Mie}$), where i is the iteration number. Each of these smoothed

310   images are checked for the availability of coherent features. In general, for ATLID, the useful range of iterations runs from 25 convolutions up to 180 subsequent convolutions. The lowest two number of convolution images are used to detect the medium strong features (FM values of 6 to 7) while the latter two are needed for very low signal to noise aerosol features (FM values of 6).

As the noise is assumed to be Gaussian, the resulting convolved noise signals are also Gaussian. The Gaussian nature of the

315   smoothed field is exploited in the next step in the algorithm where a dynamic threshold is retrieved to separate clear-sky from aerosol/cloud pixels. From the different convolved $P_{i,Mie}$ images, the one dimensional detection probability histograms are calculated. The histogram depicts the number of pixels within a signal probability bin, normalized to the histogram maximum (Figure 4). The histogram maximum is determined by the clear-sky pixels, since most of the pixels in the atmosphere do not contain enough aerosols to enhance the co-polar Mie backscatter signals. On the left side of the histogram peak one finds the

320   pixels which originally had very low or negative backscatter values which have not been smoothed enough. On the right side of the peak, one finds the pixels which have enhanced Mie backscatter values, which could in principle be associated with aerosol or low backscatter cloud returns.

In Figure 4, two example of the $P_{i,Mie}$ histograms are shown (blue lines) after 40 and 80 convolutions, respectively, with the 2D Gaussian smoothing Kernel. In order to separate the noise peak from the feature signals, as depicted on the right side

325   a multi-Gaussian fit (green line) is performed on the histogram and from this the definition of the noise peak (red line). Once the multi Gaussian fit exceeds the noise peak by more than a threshold value (i.e. 8 or 10) the clear sky versus Mie particle threshold is defined, which is depicted by the dashed line. Since the histograms and subsequently the multi-Gaussian fit differ from frame to frame this Mie particle threshold depends on the local conditions. This ensures that the final threshold used for the particle vs. molecular pixels is flexible and defined by the data, i.e. background noise, and not on a pre-defined fixed value.

330   In the Figure 4 the signals from the low signal to noise ratio pixels start with a shoulder on the noise peak (Signal probability $\approx$0.25) and shows larger deviations beyond $\approx$0.3. When the shoulder exceeds the noise peak by a factor 10 (along the y-axis) the threshold for this segment of the observed frame is determined. All pixels which make up the area on the right side of this

threshold are defined as part of a feature. Since this is a statistical approach, and holds for individual pixels it means that per definition it does not directly mean that neighboring pixels will all be selected. However, in practice, due to the smoothing,
335   neighboring pixels will have similar values and the procedure tends to fill in complete e.g. distributed aerosol regions.

2.6.1 Combining the Strong and Weak Features

As described in the previous sections, the detection of strong and weak features have been addressed using very different procedures. This may for one thing, result in potential gaps between these two types of detected features, e.g. there may be a small gap between a liquid cloud layer (detected using the HM filter approach) and the surrounding aerosols (detected using
340   the Gaussian smoothing filter approach). A second problem which can arise are small gaps in the detected weak features due to the statistical nature of the approach. A third issue has to do with the wavelength of ATLID. Since the molecular attenuation in the UV becomes significant at low altitudes due to the increasing atmospheric density profile and the relatively large molecular Rayleigh extinction cross section at 355-nm, the signal to noise ratio of ATLID signals can become especially low close to the surface. In those cases where a layer of weak features is detected close to the surface, its extent is extended to the surface with
345   a lower FeatureMask index level (FM=5). Finally, there is the chance of a gap occurring between strongly attenuating features like ice and liquid clouds in the Mie signals and the detection of attenuated areas assessed using the Rayleigh signal. In this case, the attenuated region is extended upwards to the lowest pixel with a FeatureMask value ≥ 6 within each column.

To deal with the issues just described, first a combined feature mask (CFM) is created combining the weak and strong feature mask. The integration is performed by applying the hybrid median m×m routine iteratively five times on top of the retrieved
350   combined feature mask. The resulting mask is compared to the original CFM. All features filled in due to the hybrid median filtering are added to CFM, all features disappearing receive a penalty of one to two points on their detection status.

The final retrieved FeatureMask for the signals shown in Figure 1 is shown in Figure 5. In the top panel, the FeatureMask output is shown, the bottom panel depicts which part of the algorithm the results originate from. The thick marine aerosol layer as well as the thicker ice clouds at the start of the scene are found mostly using the HM filter step. The thinner elevated aerosol
355   layer is found by the weak feature smoothing part of the algorithm (convolution images 1 to 4). The white contour lines in the top panel depict those regions for which the model-truth extinction values are equal to 1.e-6 m^{-1}. As can be seen that the upper edge of the model extinction field is closely followed in most cases (except for below the ice cloud and the upper right side).

3   Algorithm performance and sensitivity

360   Over the years many verification measures have been devised for comparing forecasts with observations that are commonly used in the field of meteorology. In this section the verification indices or scores used for the verification of the FeatureMask are described. Details of some of these methods can be found in Fuller (2004). When looking at a forecast event that either occurs or does not occur, the events can be represented by a 2x2 contingency table. Each individual event is categorical, non-probabilistic, and discrete. Examples of this type of forecast include rain versus no rain, or a severe weather warning.

365 In this case it is the detection of a feature (forecast) versus pixels where the input model does have an extinction $> 1.e\text{-}6$ m^{-1} (observed). From these contingency table a number of statistical properties can be calculated like the percent of forecasts that are correct (PC=0.91; for the scene discussed above), the hit rate (HR=0.68) or false alarm ratio (FAR=0.02) and more complex combinations of the latter like the Heidke Skill Score (HSS=0.74 Heidke, 1926). Since there are a number of detailed forward modelled ATLID signals based upon model scenes (Donovan et al., 2022a) this provides a great chance to evaluate the

370 FeatureMask algorithm in this manner and perform sensitivity tests on the available configuration parameters. In Figure 6 the fraction of detected pixels with respect to the model extinction is plotted. The green line shows that above extinction of 10^{-5} m^{-1}, most of the pixels are detected. For higher extinctions the detection rate goes slightly down again. This has to do with the attenuation of higher lying aerosol layers and/or ice clouds which reduces the SNR and therefore detectability of the layers below. The yellow dashed line indicates the fraction of missed features above the highest lying detected pixels and depicts the

375 sensitivity of detecting the top of an aerosol layer at particular extinction. Any false detection are shown in a single column at an extinction of 10^{-7} m^{-1}, since the FAR is only 0.02 and not visible here.

4   Algorithm results

4.1   Halifax scene

Specific simulated test scenes have been created from model output data in order to test the full chain of EarthCARE processors

380 (Donovan et al., 2022a). One of these scenes is called the Halifax scene. The 6000 km long frame starts over Greenland, crosses Atlantic Canada and ends in the Caribbean. The original model output is for 7 December 2015, but for test purposes the scene is dated 31 December 2024, 18:48:08 UTC. The scene starts with clouds over the Greenland ice sheet followed by high backscatter/extinction clouds down to 50° N. A high-altitude-ice-cloud regime starting over Atlantic Canada down to 35° N is followed by a low-level cumulus cloud regime embedded in a marine aerosol layer below an elevated continental pollution layer

385 around an altitude of 5 km. The aerosol scene discussed earlier is based on the last part of this scene. The cloud information comes from high resolution GEM model output (Qu et al., 2022) while the aerosol information is taken from the CAMS model Peuch et al. (2022).

In Figure 7, the Halifax scene is shown in more detail, starting with the model input extinction field. The forward modelled co-polar Mie and Rayleigh field and finally the retrieved FeatureMask following the methods described above.

390 Most of the features present in the Halifax scene can be directly seen back in the FeatureMask, where the top of the features nicely follow the extinction field values around $\approx 10^{-6}$ m^{-1} except from the very optically thin aerosol layer between latitudes of 63 and 51^oN and altitude between 5 and 6 km. By eye, one can distinguish this tenuous aerosol region, but the smoothing routines can not bring the feature with an average AOD of 0.007 (mean extinction $5.9 \cdot 10^{-6}$ m-1 and maximum extinction of $9.0 \cdot 10^{-6}$ m-1, is too tenuous to be retrieved as a continuous feature and only a few pixels are found. In general the retrieval

395 nicely follows the edges of the features and there are relatively few false alarms (FAR: 0.01), a relatively high hit rate (HR=0.76) and Heidke skill score (HSS=0.81).

Another way to show whether all features have been detected is by averaging horizontally all pixels that are classified as (likely) clear-sky (FM values 0 to 4) with no detected feature pixels present above. What one should expect is, that in the case of a clear atmosphere, that there are no Mie scatterers, i.e. the average Co-Polar Mie channel signals should be 0 at 400 all altitudes. The Total cross polar profile however includes the Rayleigh cross polarization, which is directly related to the molecular density itself. The clear sky signal for the cross-polar channel should thus follow a scaled atmospheric density profile corrected for the Rayleigh transmission profile. In Figure 8, the three clear sky profiles for the three channels are shown. The Mie signals oscillate around 0 above 9 km and shows an enhancement of 1.5E-8 $sr^{-1}m^{-1}$ between 5 and 10 km. This signal mostly originates from the missing feature (discussed above and the upper edge of the aerosol region in the right side of 405 the image around latitude of 30.3 ^{o}N. The Rayleigh channel follows the density profile until the increasing molecular density impacts the signals at 355 nm due to attenuation. The cross-polar channel follows a scaled Rayleigh profile indicating that the signal is directly coming from the linear cross polarization from the molecular backscatter. It does show that no features have been missed containing ice particles or dust like aerosols. Both the co-polar Mie and total cross-polar channel do show enhancements in the lower kilometer, these signals come from regions which have no detected features and on top of this have 410 relatively low attenuated backscatter values thanks to the molecular attenuation at 355 nm. These profiles are standard outputs from the processor and will to be used for checking the cross calibration performed for the ATLID instrument L1b processor once EarthCARE is in space.

As previously explained, one of the main reasons for the FeatureMask is to guide the implementation of smoothing strategies for, especially, optically thin features. Not only the separation of strong and weak features is of importance, but ot is also 415 necessary to ensure that no surface signals are mixed with aerosol signals when calculating aerosol optical properties. In Figure 9, a zoomed view is provided for the area around the detected pixels affected by surface returns in the Halifax scene. Shown are the 16 pixels around the detected lidar surface pixel for each profile, indicated by S, the retrieved FeatureMask for these pixels and the statistical properties of the surface and adjacent vertical pixels. The lidar surface pixel can in general be detected by eye in the figure as the strongest signal within the profiles that occurs either at pixel index [S] or [S-1] in case 420 the pixel above the actual surface is deemed to be influenced by the surface backscatter, see Section 2.3 for the description of surface detection. Statistically the pixel above the surface return shows a similar attenuated backscatter histogram to the surface pixel and the pixel below the detected surface between $10^{-9} < \beta_{Mie} < 10^{-4}m^{-1}sr^{-1}$, however the latter two also peak at higher backscatter values due to the surface returns. In those cases where the pixels below the lidar surface have a higher absolute value it is assumed that the detected lidar surface pixel is still dominated by the true surface. The lack of strong 425 signals in the pixel above the lidar surface return indicates that these can be safely used when smoothing signals. Note that on the right side of the FeatureMask, over the Caribbean, the low altitude aerosol pixels are indicated in grey. These pixels have been set to a FeatureMask value of 5 due to the overlying aerosol pixels, not by their absolute signals themselves. The atmospheric attenuation at 355nm often extincts the signals while it is likely that the aerosol field is extended all the way to the surface. By separating these pixels this way it provides users of the product to choose whether the underlying signals should 430 be used for their specific needs or not.

4.2 Using Aeolus data for evaluating the A-FM methods.

In August 2018 the European Space Agency (ESA) launched the Aeolus Earth Explorer Mission (Reitebuch et al., 2019, 2020). Aeolus caries an ultraviolet UV high-spectral resolution lidar, the Atmospheric LAser Doppler INstrument (ALADIN). AL-ADIN, like ATLID, measures the atmospheric backscatter from air molecules and particles in separate channels, however, the ALADIN instrument is optimized to measure the line-of-sight (los) wind profile observations in the troposphere and lower stratosphere. The los wind component is measured by detecting the Doppler shift induced by the atmospheric movements with respect to the satellite. The main detection channels aboard ALADIN are referred to as the Mie and Rayleigh channels (the Rayleigh channel itself is comprised of two spectral filter elements). In the Mie channel the signal is detected in a spectrally resolved manner and the wavelength shift of the particle backscatter can be detected. The molecular signals are detected using two offset Rayleigh channels each covering one of the wings of the thermally broadened molecular backscatter returns. The ratio of these wings is used to measure the Doppler shift of the local molecules, i.e. the los wind component.

To improve the signal to noise ratio of the signals a relatively low range resolution (minimum 250 m up to 2 km) and low number of vertical bins are available (24) up to in general 20 km. The per-bin vertical resolution of the 24 bins can be controlled and changed within an orbit. Atmospheric optical properties are provided as second order product, however, being an HSRL, ALADIN is able to independently retrieve the particle extinction, co-polarized particle backscatter coefficients and therefore the co-polarized lidar ratio, the cross-polarized return signal is not measured.

The ALADIN data provides an opportunity for testing the FeatureMask as described in this paper. The procedures described within this paper relies on edge detection and smoothing in both the horizontal and the vertical and was not designed with a small number of vertical pixels and changing resolution within the profile but also between subsequent profiles. In order to create signals which can be used by the FeatureMask algorithm, the data is first transformed to a constant vertical resolution grid starting at the lowest altitude within the orbit up to the maximum altitude of the Mie grid for that orbit.

For those pixels that are distributed over multiple vertical bins, within the newly defined high resolution grid, the low resolution signals have an added random normal component using the errors reported in the Aeolus L1 product. The main reason for this step is to ensure that single high backscatter returns with relatively large errors do not spread out over a large number of pixels but have values related to the local error estimates. The high resolution Rayleigh and Mie signals are subsequently fed into the FeatureMask procedure as described earlier. The resulting high resolution retrieved FeatureMask is finally downgraded to the original grid adopting the highest retrieved FeatureMask value when multiple pixels are combined within a low resolution pixel. The resulting procedure has been added to the current Aeolus operational L2a processor Flament et al. (2021) as the Feature_Mask_Index from the AEL-FM processor output. It has been providing operational results since version 3.15 from mid 2022 together with the first version of the AEL-PRO processor, which is the Aeolus version of the A-PRO (Donovan et al., 2022b) processor. This nicely shows how procedures developed for one ESA explorer mission can be adapted for other missions. In Figure 10 a comparison of the AEL-FM results is shown for a collocated Aeolus overpass with CALIPSO. The time difference between the two missions is roughly four hours and obviously specific features will have changed in the mean time. However, in those cases where long lived events are present, the FeatureMask results can still be

15

465 evaluated against the high resolution CALIOP retrievals. In this particular case, the two satellites fly over the tip of Somalia (east Africa) towards Yemen on May 1st 2019. There is a thick dust layer up to an altitude of 5 km surrounded by ice clouds. Over the Indian Ocean (left side of the image a number of liquid clouds are visible with low level marine aerosols. On the right side the CALIPSO signals and VFM mask (Vaughan et al., 2009) show liquid cloud layers which are not visible in the Aeolus data. This can either be due to the difference in overpass time or that the two observation sheets are not fully collocated in

470 space. Both the dust and ice clouds are nicely captured by both the FeatureMask and the VFM mask and can be seen by eye in the respective L1 images. A number of these cases are currently being examined in terms of both the detectability as well as the detailed retrieval of microphysical aerosol and cloud properties as part of the Aeolus L2 evaluation.

5 Conclusions

The Earth Clouds Aerosol and Radiation Explorer (EarthCARE) mission is a combined ESA/JAXA mission to be launched
475 in 2024 and has been designed with sensor-synergy playing a key role to retrieve cloud, aerosol and radiation products and enabling the study of the interactions between the three. A system of 17 geophysical algorithms (L2) have been designed to work in a chain to perform the best possible 3D reconstruction of the cloud and aerosol atmospheric state.

In this paper the ATLID feature mask algorithm (A-FM) has been described, the main task of which is to separate regions with particle returns from molecular backscatter regions only. It is the first processor in the ATLID HSRL chain and the only
480 one providing its results at the native lidar grid. The output FeatureMask enables the ATLID profile retrieval processor (A-PRO) to design optimal binning strategies to minimize the number of shots required for reaching high enough SNR and ensure that no clear sky and strong surface or cloud backscatter returns are mixed with tenuous aerosol or ice cloud layers. A-FM has been based on a number of (statistical) image reconstruction techniques.

One of the first steps performed is the detection of the surface mask, which includes all pixels affected by the surface
485 backscatter. The current implementation has been conservative in the sense that all pixels above the surface which have a high enough elevated backscatter signal with respect to the pixels above are classified as surface return contaminated. This may include near surface feature occurrence within a few 100 meters from the surface, i.e. fog and blowing snow. Once enough ATLID data is available an attempt will be made to improve upon the surface mask and provide an improved low height feature detection. Next to this mask, the integrated surface returns are written out which in the future are intended to be directly used
490 in the retrieval of aerosol optical depth (AOD) from the lidar signal reflected from the sea surface (e.g. He et al. (2016)).

The A-FM algorithm has been evaluated thoroughly using the synthetic test scenes (Donovan et al., 2022a, ECSIM)) and ALADIN L1 data from the Aeolus wind-lidar mission. The test scenes allow for a direct comparison of the resulting Feature-Mask to the 2D model 'truth' fields used as input to the simulator. These comparisons indicates that the mask has a percentage correctness >0.9 and is capable of reliably detecting aerosol regions with extinctions $> 1E\text{-}5 \ m^{-1}$.

495 For the Aeolus mission, the A-FM processor has been reformed into the operational Aeolus FeatureMask (AEL-FM) processor which is part of the official level 2a Aeolus processor. The AEL-FM contains most of the core elements of the A-FM

processor, and its successful implementation and subsequent evaluation based on more than 1 year of data provides good insight into the processor core and its capabilities.

Finally, the A-FM outputs will provides a direct way to evaluate the ATLID channel calibration in the L1b data. For the 500 L1b verification, the average clear sky signal profiles for the three ATLID channels, the Co-Polar Mie, total Cross polar and Co-Polar Rayleigh channel have been created. These profiles will indicate for each frame whether the Calibration of all cross talk parameters has been well performed.

Author contributions. All authors of this paper, namely Gerd-Jan van Zadelhoff, David P. Donovan and Ping Wang contributed fairly with 510 regard to the development of the studies that led to the results presented here. They also contributed equally to the writing/correction of the different parts of the paper for which they are responsible.

Competing interests. The authors declare that they have no conflict of interest.

References

Barker, H. W., Cole, J. N. S., Qu, Z., Villefranque, N., and Shephard, M.: Radiative closure assessment of retrieved cloud and aerosol properties for the EarthCARE mission: the ACMB-DF product, Atmospheric Measurement Techniques, to be submitted, 2022.

do Carmo, J. P., de Villele, G., Wallace, K., Lefebvre, A., Ghose, K., Kanitz, T., Chassat, F., Corselle, B., Belhadj, T., and Bravetti, P.: ATmospheric LIDar (ATLID): Pre-Launch Testing and Calibration of the European Space Agency Instrument That Will Measure Aerosols and Thin Clouds in the Atmosphere, Atmosphere, 12, https://doi.org/10.3390/atmos12010076, 2021.

Donovan, D., Kollias, P., van Zadelhoff, G.-J., and Velázquez-Blázquez, A.: The Generation of EarthCARE L1 Test Data sets Using Atmospheric Model Data Sets, Atmospheric Measurement Techniques, to be submitted, 2022a.

Donovan, D., van Zadelhoff, G.-J., and Wang, P.: The ATLID L2a profile processor (A-AER, A-EBD, A-TC and A-ICE products), Atmospheric Measurement Techniques, to be submitted, 2022b.

Eisinger, M., Wehr, T., Kubota, T., Bernaerts, D., and Wallace, K.: The EarthCARE Mission - Science Data Processing Chain Overview, Atmospheric Measurement Techniques, to be submitted, 2022.

Flament, T., Trapon, D., Lacour, A., Dabas, A., Ehlers, F., and Huber, D.: Aeolus L2A aerosol optical properties product: Standard correct algorithm and Mie correct algorithm, Atmospheric Measurement Techniques, 14, 7851–7871, https://doi.org/10.5194/amt-14-7851-2021, 2021.

Fuller, S.: Forecast verification: A practitioner's guide in atmospheric science. Edited by Ian T. Jolliffe and David B. Stephenson. Wiley, Chichester, 2003. xiv+240 pp. ISBN 0 471 49759 2, Weather, 59, 132–132, 2004.

Grigas, T., Maxime, H., Gimmestad, G., Forrister, H., Schneider, P., Preißler, J., Tarrason, L., and O'Dowd, C.: CALIOP near-real-time backscatter products compared to EARLINET data, Atmospheric Chemistry and Physics, 15, https://doi.org/10.5194/acp-15-12179-2015, 2015.

He, M., Hu, Y., Huang, J. P., and Stamnes, K.: Aerosol optical depth under "clear" sky conditions derived from sea surface reflection of lidar signals, Opt. Express, 24, A1618–A1634, https://doi.org/10.1364/OE.24.0A1618, 2016.

Heidke, P.: Berechnung des Erfolges und der Gute der Windstarkevorhersagen im Sturmwarnungsdienst, Geogr. Ann., 8, 301–349, 1926.

Herzfeld, U., Hayes, A., Palm, S., Hancock, D., Vaughan, M., and Barbieri, K.: Detection and Height Measurement of Tenuous Clouds and Blowing Snow in ICESat-2 ATLAS Data, Geophysical Research Letters, 48, e2021GL093473, https://doi.org/https://doi.org/10.1029/2021GL093473, e2021GL093473 2021GL093473, 2021.

Illingworth, A. J., Barker, H. W., Beljaars, A., Ceccaldi, M., Chepfer, H., Clerbaux, N., Cole, J., Delanoë, J., Domenech, C., Donovan, D. P., Fukuda, S., Hirakata, M., Hogan, R. J., Huenerbein, A., Kollias, P., Kubota, T., Nakajima, T., Nakajima, T. Y., Nishizawa, T., Ohno, Y., Okamoto, H., Oki, R., Sato, K., Satoh, M., Shephard, M. W., Velázquez-Blázquez, A., Wandinger, U., Wehr, T., and van Zadelhoff, G.-J.: The EarthCARE Satellite: The Next Step Forward in Global Measurements of Clouds, Aerosols, Precipitation, and Radiation, Bulletin of the American Meteorological Society, 96, 1311–1332, https://doi.org/10.1175/BAMS-D-12-00227.1, 2015.

Irbah, A., Delanoe, J., Zadelhoff, G.-J., Donovan, D., Kollias, P., Tatarevic, A., Treserras, B. P., Mason, S., and Hogan, R.: The classification of atmospheric hydrometeors and aerosols from EarthCARE radar and lidar: the A-TC, C-TC and AC-TC products, Atmospheric Measurement Techniques, 2022, https://doi.org/https://doi.org/10.5194/egusphere-2022-1217, 2022.

Markus, T., Neumann, T., Martino, A., Abdalati, W., Brunt, K., Csatho, B., Farrell, S., Fricker, H., Gardner, A., Harding, D., Jasinski, M., Kwok, R., Magruder, L., Lubin, D., Luthcke, S., Morison, J., Nelson, R., Neuenschwander, A., Palm, S., Popescu, S., Shum, C., Schutz,

B. E., Smith, B., Yang, Y., and Zwally, J.: The Ice, Cloud, and land Elevation Satellite-2 (ICESat-2): Science requirements, concept, and
550   implementation, Remote Sensing of Environment, 190, 260–273, https://doi.org/https://doi.org/10.1016/j.rse.2016.12.029, 2017.

Mason, S., Hogan, R. J., Bozzo, A., and Pounder, N.: A unified synergistic retrieval of clouds, aerosols and precipitation from EarthCARE:
       the ACM-CAP product, Atmospheric Measurement Techniques, to be submitted, https://doi.org/https://doi.org/10.5194/egusphere-2022-
       1195, 2022.

Peuch, V.-H., Engelen, R., Rixen, M., Dee, D., Flemming, J., Suttie, M., Ades, M., Agustí-Panareda, A., Ananasso, C., Andersson, E.,
555   Armstrong, D., Barré, J., Bousserez, N., Dominguez, J. J., Garrigues, S., Inness, A., Jones, L., Kipling, Z., Letertre-Danczak, J., Par-
       rington, M., Razinger, M., Ribas, R., Vermoote, S., Yang, X., Simmons, A., de Marcilla, J. G., and Thépaut, J.-N.: The Copernicus
       Atmosphere Monitoring Service: From Research to Operations, Bulletin of the American Meteorological Society, 103, E2650 – E2668,
       https://doi.org/10.1175/BAMS-D-21-0314.1, 2022.

Qu, Z., Donovan, D. P., Barker, H. W., Cole, J. N. S., Shephard, M., and V., H.: Numerical model generation of test frames for pre-launch
560   studies of EarthCARE's retrieval algorithms and data management system, Atmospheric Measurement Techniques Discussions, 2022,
       https://doi.org/https://doi.org/10.5194/amt-2022-300, 2022.

Reitebuch, O., Lemmerz, C., Lux, O., Marksteiner, U., Rahm, S., Weiler, F., Witschas, B., Meringer, M., Schmidt, K., Huber, D., Nikolaus, I.,
       Geiss, A., Vaughan, M., Dabas, A., Flament, T., Stieglitz, H., Isaksen, L., Rennie, M., de Kloe, J., Marseille, G.-J., Stoffelen, A., Wernham,
       D., Kanitz, T., Straume, A.-G., Fehr, T., von Bismark, J., Floberghagen, R., and Parrinello, T.: Initial assessment of the performance of the
565   first Wind Lidar in space on Aeolus, in: International Laser Radar Conference 19, https://doi.org/10.1051/epjconf/202023701010, 2019.

Reitebuch, O., Krisch, I., Lemmerz, C., Lux, O., Marksteiner, U., Masoumzadeh, N., Weiler, F., Witschas, B., Bracci, F., Meringer, M.,
       Schmidt, K., Huber, D., Nikolaus, I., Fabre, F., Vaughan, M., Reisig, K., Dabas, A., Flament, T., Lacour, A., Mahfouf, J.-F., Trapon, D.,
       Savli, M., Abdalla, S., Isaksen, L., Rennie, M., Donovan, D., de Kloe, J., Marseille, G.-J., Stoffelen, A., Perron, G., Jupin-Ganglois, S.,
       Smeets, J., Veneziani, M., Bucci, S., Gostinicchi, G., Ehlers, F., Kanitz, T., Straume, A.-G., Wernham, D., von Bismarck, J., Bley, S.,
570   Fischer, P., Laurentis, M. D., and Parinello, T.: Assessment of the Aeolus performance and bias correction - results from the Aeolus DISC,
       in: Aeolus Cal/Val and Science Workshop, https://elib.dlr.de/138648/, 2020.

Rush, J. C.: The Image Processing Handbook, CRC Press, 5th edn., 2007.

Smith, C. R. and Grandy, W. T. J.: Maximum-Entropy and Bayesian Methods in Inverse Problems, in: Maximum-Entropy and Bayesian
       Methods in Inverse Problems, 1985.

575 Vaillant de Guélis, T., Vaughan, M. A., Winker, D. M., and Liu, Z.: Two-dimensional and multi-channel feature detection algorithm for the
       CALIPSO lidar measurements, Atmospheric Measurement Techniques, 14, 1593–1613, https://doi.org/10.5194/amt-14-1593-2021, 2021.

Vaughan, M. A., Powell, K. A., Winker, D. M., Hostetler, C. A., Kuehn, R. E., Hunt, W. H., Getzewich, B. J., Young, S. A., Liu, Z., and
       McGill, M. J.: Fully Automated Detection of Cloud and Aerosol Layers in the CALIPSO Lidar Measurements, Journal of Atmospheric
       and Oceanic Technology, 26, 2034–2050, https://doi.org/10.1175/2009JTECHA1228.1, 2009.

580 Wehr, T., Kubota, T., Tzeremes, G., Wallace, K., Nakatsuka, H., Ohno, Y., Koopman, R., Rusli, S., Kikuchi, M., Eisinger, M., Tanaka, T.,
       Taga, M., Deghaye, P., Tomita, E., and Bernaerts, D.: The EarthCARE Mission - Science and System Overview, Atmospheric Measurement
       Techniques, to be submitted, 2022.

Winker, D. M., Vaughan, M. A., Omar, A., Hu, Y., Powell, K. a., Liu, Z., Hunt, W. H., and Young, S. a.: Overview of the
       CALIPSO Mission and CALIOP Data Processing Algorithms, Journal of Atmospheric and Oceanic Technology, 26, 2310–2323,
585   https://doi.org/10.1175/2009JTECHA1281.1, 2009.
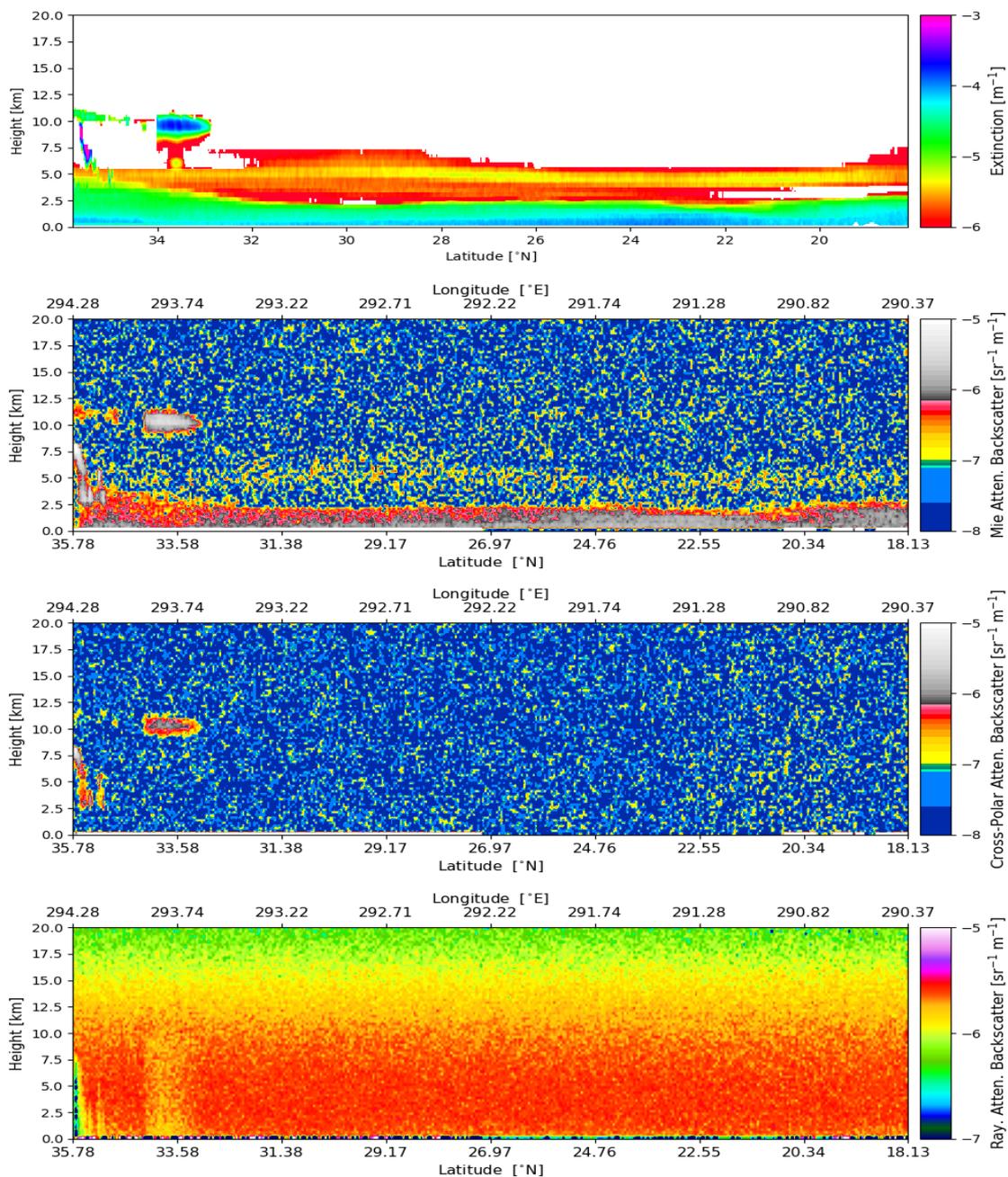
Figure 1. The model extinction field used to create the EarthCARE signals (top panel) with the forward modelled ATLID signals for the Co-polar Mie (2nd), Cross total (3rd) and Co-polar Rayleigh (bottom) channels. The scene consists of a thick aerosol layer ($\tau \approx 0.28$) in the bottom 2 km (light green color in top panel), a thin aerosol later between 4 and 6 km ($\tau \approx 2.2$e-2; red to yellow color in top panel) and a few ice clouds at the start of the scene.
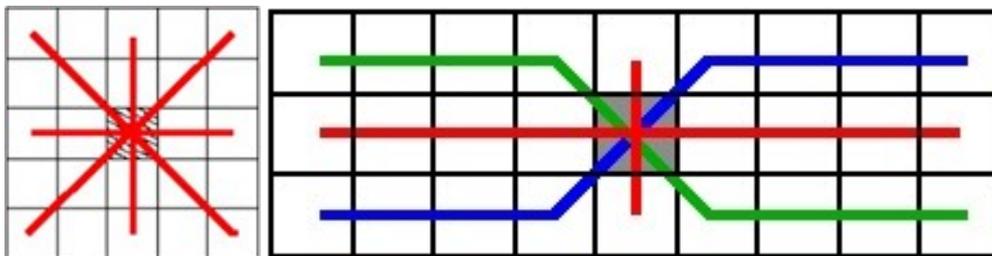
Figure 2. Two examples of hybrid median kernels used for finding strong features. The left panel shows a square filter of 5x5 and on the right an example of a horizontal oriented kernel (9x3). The thick lines depict the pixels for which the median values in the center pixel are calculated.
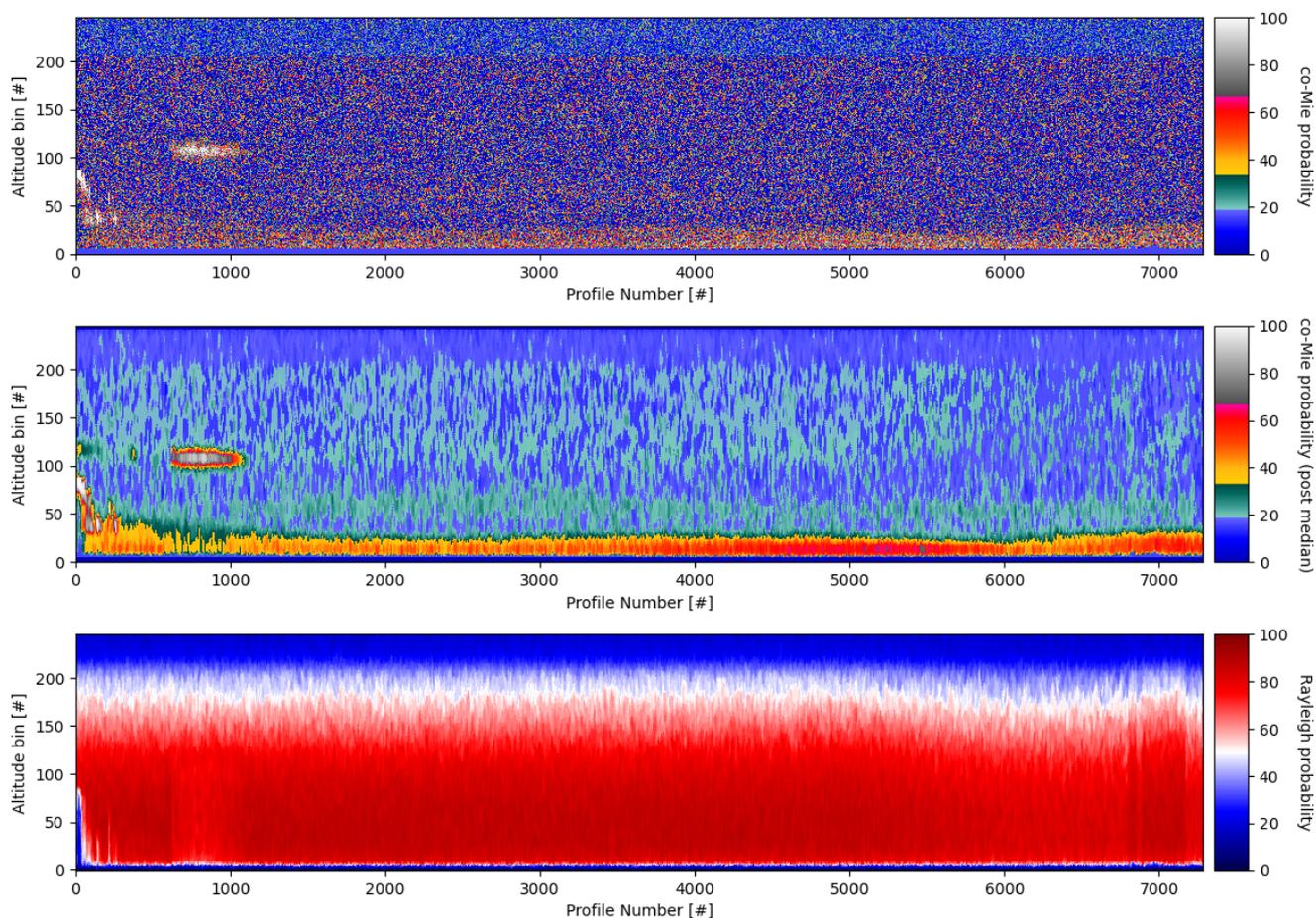
Figure 3. The top figure depicts the Co-polar Mie signal probabilities from Equation 4 using the signals shown in Figure 1. The center plot is the resulting image after the Hybrid median routine adopting an 11x11 size square filer, any additional found pixels in thin layers were detected using an 11x3 horizontal oriented Hybrid median filter. The bottom plot represents the Rayleigh channel signal probabilities. Note that the figure is shown in pixel number since the procedure is defined in pixel number count and not in SI units of length
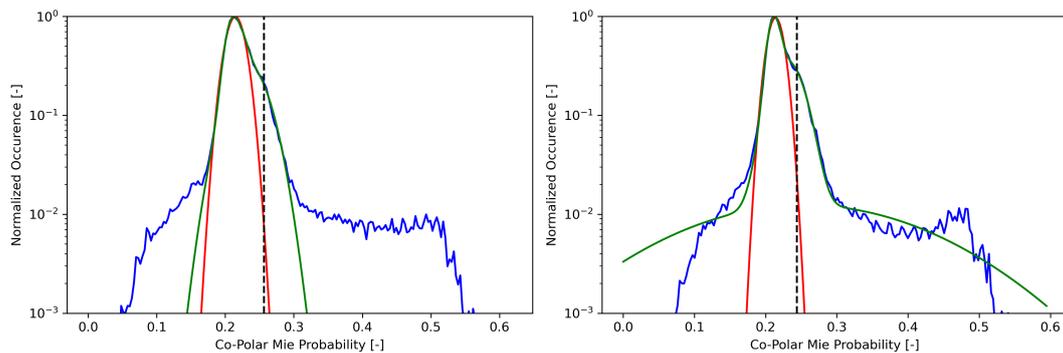
Figure 4. Example of two of the probability histograms for one of the regions after 40 and 80 convolutions. The blue lines show the smoothed probability data, the green lines the multi-Gaussian fit and the dashed black line the retrieved threshold P_t. The red line depicts the fit of the central Gaussian noise peak. All pixels with a probability $P_{i,Mie} > P_t$ are retrieved as part of a Feature.
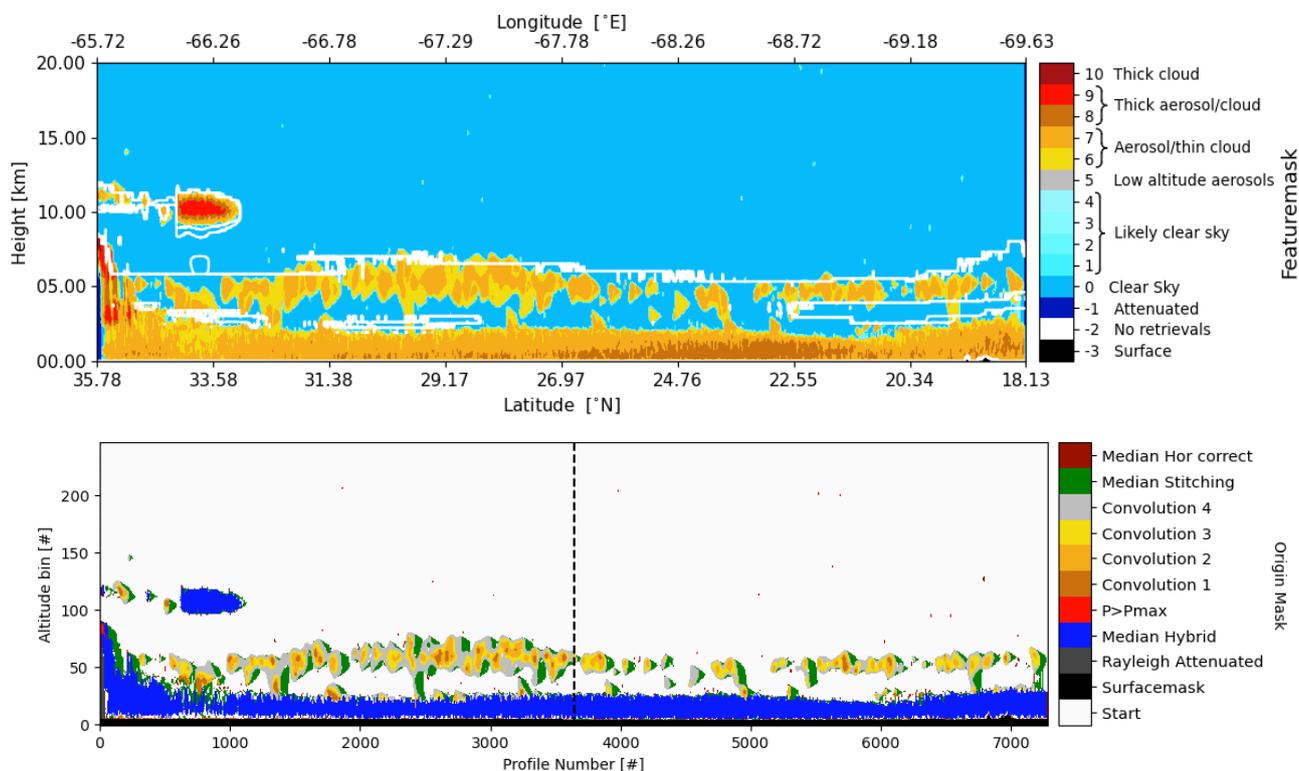
Figure 5. FeatureMask results for the signals shown in Figure 1. The top panel shows the FeatureMask (filled in contours) with on top the white contour lines depicting an extinction of 1.e-6 m^{-1} of the input model fields. The bottom panel indicates for each pixel from which part of the processor the results originate. Since all procedures are performed in 'pixel' space the lower image is shown in the profile and altitude number count, note that the latter reach the full 40 km height and has not been cut of at 20 km. The dashed line indicates the two regions which were retrieved in parallel by the algorithm.
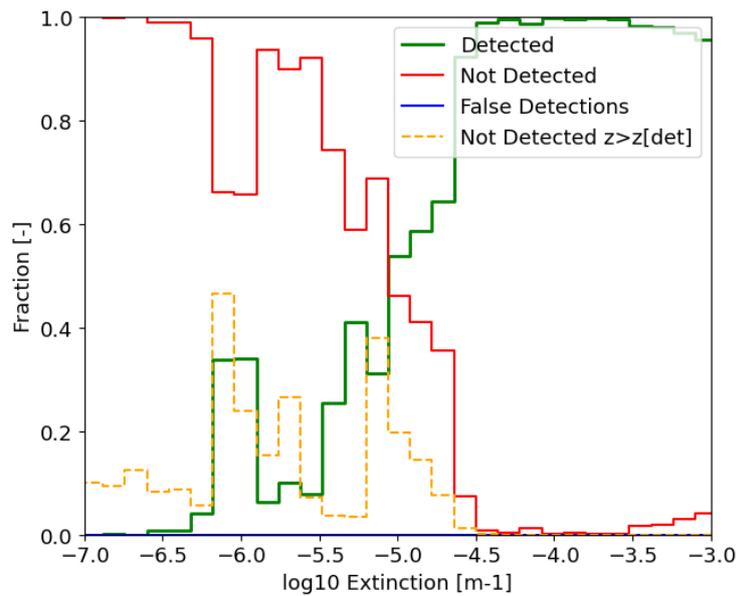
Figure 6. Fraction of detected (green line) and undetected pixels (red) with respect to the input model extinction fields which was used to forward model the ATLID L1b signals. The yellow dashed line shows the fraction off undetected pixels above the highest detected pixel within each column.
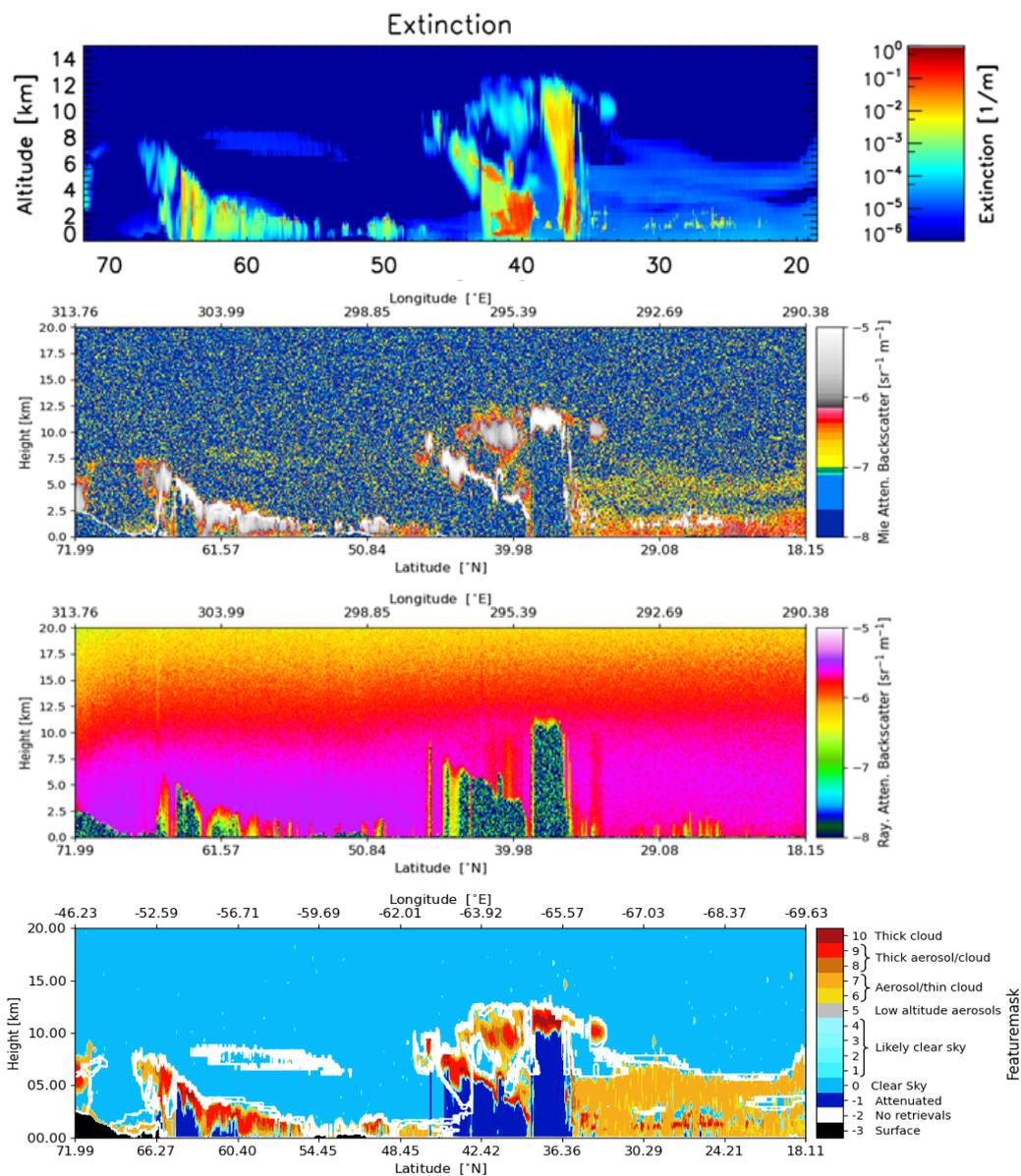
Figure 7. Halifax scene; top panel shows the input model extinction field, 2nd panel the forward modelled Mie Co-Polar and 3rd the forward modelled Co-Polar Rayleigh attenuated backscatter signals. The bottom panel depicts the retrieved FeatureMask for this scene with on top the $\alpha=10^{-6}$ m^{-1} extinction contours in white. Note that the model truth has a different verticals scale to highlight the variations in extinction better.

26
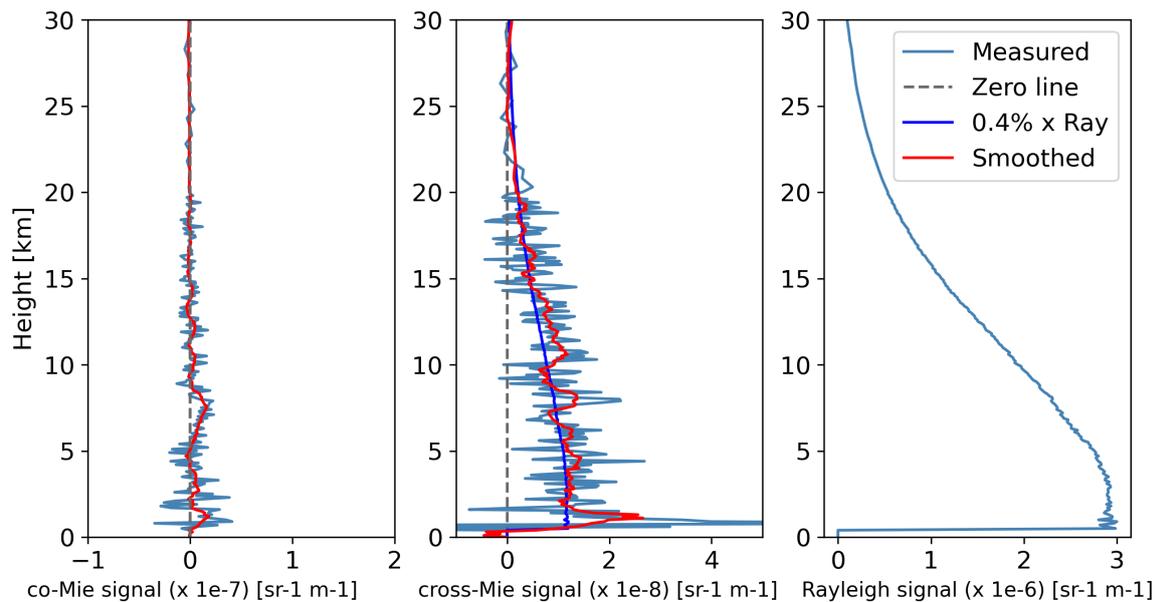
Figure 8. Profiles of the average clear sky signals for the Co-Polar Mie, total Cross polar channel and Co-Polar Rayleigh channel from left to right. For each plot the average of the entire segment is shown in light blue, a vertically smoothed profile in red and in case of the cross polar channel the scaled Rayleigh profile in dark blue.
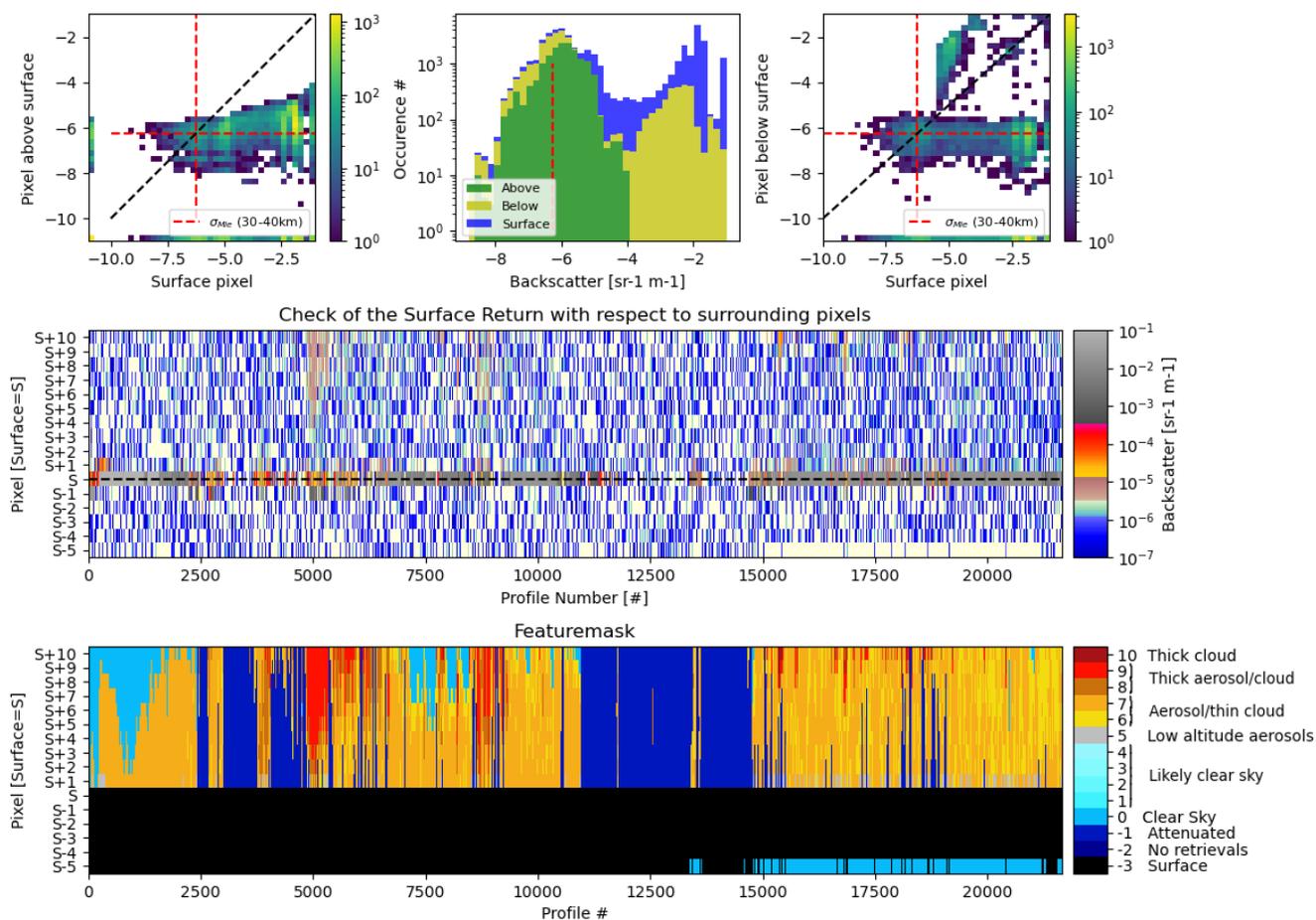
Figure 9. Detection of the surface for the Halifax scene following the description in section 2.3. The center panel shows the Mie co-polar returns at native resolution in the 16 pixels around the retrieved surface pixel [S]. The bottom panel shows the subsequent FeatureMask for these pixels. The top three panel provide the 2D histograms of signal occurrence of the surface pixel with respect to the pixel above (left) and pixel below (right), with the dashed red line indicating the co-polar Mie noise levels between 30 and 40 km and the black dashed line the one-to-one line. The top-center panel provides the 1D histograms of signal occurrence for the surface-pixels and the pixels above and below the surface pixel.
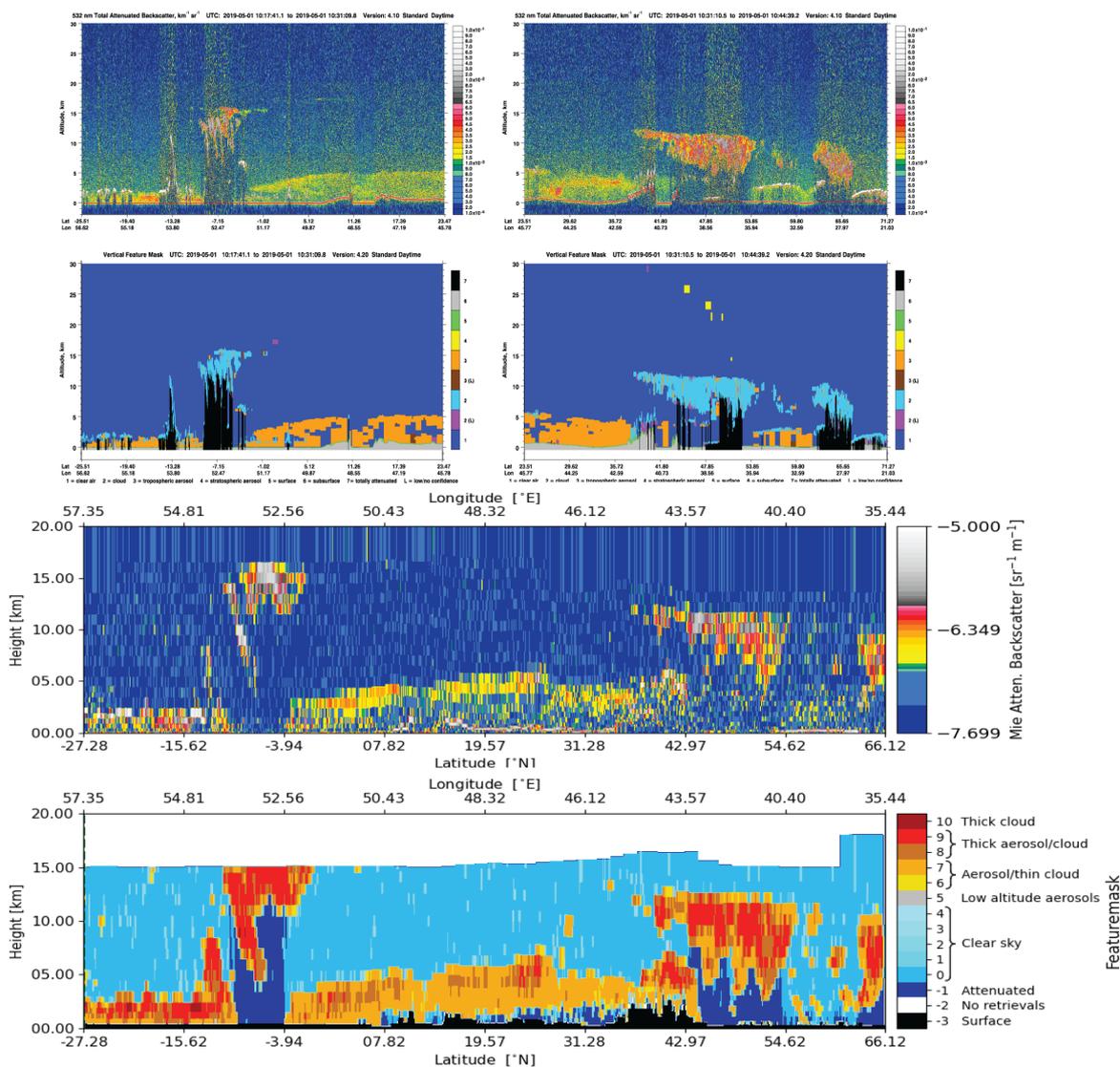
Figure 10. Comparison of a CALIPSO and Aeolus overpass (Orbit 3991) on 2019-05-01 over the tip of Somalia (east Africa) towards Yemen. The top panels show the CALIPSO 532nm backscatter quicklooks with the second row the corresponding VFM mask. The third and bottom rows show the 355nm Aeolus backscatter and AEL-FM results for the overpass a few hours later. Both the dust layer and ice clouds are clearly visible in both instrument L1 data and retrieved by their respective feature finders.